Review

A basic introduction to single particles cryo-electron microscopy

Vittoria Raimondi[1] and Alessandro Grinzato[2,3]*

[1] Veneto Institute of Oncology IOV – IRCCS, via Gattamelata 64, 35128, Padova, Italy
[2] Department of Biomedical Sciences, University of Padova, Via Ugo Bassi 58b 35131 Padova, Italy
[3] Present address: ESRF, The European Synchrotron, 71 Avenue des Martyrs, 38043 Grenoble, France[a]

* Correspondence: Email: alessandro.grinzato@esrf.fr; Tel: +330476882557.

Abstract: In the last years, cryogenic-electron microscopy (cryo-EM) underwent the most impressive improvement compared to other techniques used in structural biology, such as X-ray crystallography and NMR. Electron microscopy was invented nearly one century ago but, up to the beginning of the last decades, the 3D maps produced through this technique were poorly detailed, justifying the term "blobbology" to appeal to cryo-EM. Recently, thanks to a new generation of microscopes and detectors, more efficient algorithms, and easier access to computational power, single particles cryo-EM can routinely produce 3D structures at resolutions comparable to those obtained with X-ray crystallography. However, unlike X-ray crystallography, which needs crystallized proteins, cryo-EM exploits purified samples in solution, allowing the study of proteins and protein complexes that are hard or even impossible to crystallize. For these reasons, single-particle cryo-EM is often the first choice of structural biologists today. Nevertheless, before starting a cryo-EM experiment, many drawbacks and limitations must be considered. Moreover, in practice, the process between the purified sample and the final structure could be trickier than initially expected. Based on these observations, this review aims to offer an overview of the principal technical aspects and setups to be considered while planning and performing a cryo-EM experiment.

Keywords: Cryo-EM; electron microscope; sample preparation; data analysis

---

[a] regarding affiliation the writing work started at Università di Padova and ended at ESRF.

1. Introduction

Nowadays, cryogenic-electron microscopy (cryo-EM) is routinely used for structural biology studies, most of which involve flexible and functionally active macromolecules [1,2]. Despite the recent success of this technique, recognized by the awarding of the 2017 Nobel Prize for chemistry to Jacques Dubochet, Joachim Frank, and Richard Henderson, the first electron microscope was developed in 1933 by Max Knoll and Ernst Ruska [3], who broke the light microscope limits. However, in the beginning, electron microscopy (EM) was not optimized for biological samples imaging. This is because there are two main drawbacks of using EM to image macromolecule samples: i) it is impossible to preserve a biological sample in the high vacuum, a condition necessary inside the electron microscope column, and ii) the biological samples could be destroyed by the beam generated by highly energetically electron-matter interaction.

Therefore, for many decades, the only way to observe biological samples was to stain them with heavy-metal salts (negative stain, NS), which unfortunately allowed to obtain only a low-resolution image of the envelope of the sample [4]. However, NS contributed to understanding the morphology of big biological complexes and providing the first images of viruses [5,6].

Later, in 1981, Jacques Dubochet and Alasdair McDowall introduced the rapid cryo-cooling of molecules in a thin ice layer of vitrified [7–9], sanctioning the birth of cryo-EM. This step revolutionized the role of EM in structural biology, as vitrification not only maintains the samples in a close-to-native environment but also protects them from dehydration and helps reduce damages caused by the electron beam.

Unfortunately, ice-embedded samples have low contrast and considerable noise, making it hard to reconstruct 3D images from 2D projections at random angles. Nevertheless, the implementation of computational processing, pioneered by Joachim Frank and Marin van Heel [10,11], allowed to extract 3D information from noisy cryo-EM. Next, many groups developed new computational image processing algorithms [12–17], and user-friendly software were helped by the constantly increasing computational power [18–21].

Concomitantly, the development of direct electron detectors [22–25] dramatically improved the images quality and the acquisition time, making it possible to trace the motion of the particles in the vitreous ice during data acquisition [26,27].

These technical improvements, alongside the development of a new generation of high-end electron microscopes designed to operate with cryogenic samples, led to the so-called "resolution revolution" [28,29]. This resulted in the last years in an exponential increase of structures deposited to the electron microscopy data bank (EMDB) [30], including important biological structures that could not have been solved by X-ray crystallography, such as large dynamic assemblies and membrane protein complexes. In this scenario, the achieved resolution has also steadily increased, and the current reported limits are 1.2 Å for single particles [31], 1.9 Å for rod shape viruses [32], and 2.2 Å for flexible filaments [33].

It is worth mentioning that cryo-EM does not require the crystallization of samples, making it advantageous over crystallography for flexible and heterogeneous samples whose intrinsic features prevent crystallization. Moreover, single-particle cryo-EM can identify individual conformational states, providing direct information about the system dynamics.

These peculiarities of cryo-EM are reported in several studies. Excellent examples are represented by the structures of the tetanus neurotoxin (TeNT), for which the use of cryo-EM not only allows to

obtain a density map but traces and describes the intrinsic flexibility of TeNT in different environmental conditions [34,35]. On the other hand, an example of the quantification of sample heterogeneity is well described by Sobti [36], where three different discrete rotational states of ATP synthase were characterized within the same dataset.

Based on these observations, this review is aimed to briefly illustrate the principles of cryo-EM, starting from the preparation of the samples to data acquisition and processing.

2. Sample preparation

Every structural biology experiment, including cryo-EM ones, first requires a high-grade purified protein sample in solution, with a concentration ranging from 10 mg/ml to 0.01 mg/ml, depending on sample characteristics [37]. Then, the sample is applied to an EM grid and blotted with filter paper to remove any excess. Next, the blotted EM grid is rapidly plunged freeze into liquid ethane (−180 °C), keeping cold by liquid nitrogen (−196 °C) [9]. This procedure freezes the sample in its native, hydrated state and, at the same time, maintains the ice layer at cryogenic temperature, which englobes the proteins and partially protects them from the radiation damage effects [38].

The quality of the vitrified specimen strongly influences the results of data collection. Indeed, a perfect vitrified sample is characterized by an amorphous ice layer that embeds the particles inside. If the ice layer appears too thick, the contrast of the particles will be too low, making complex the subsequent process of particle picking. Moreover, if the particles are embedded in a thick layer of ice, they can also overlap in the 2D projection, making it impossible to separate them from each other [39]. On the contrary, if the ice layer is too thin, it is possible to have a tiny number of particles in the hole and/or to have many particles exposed to the vacuum of the microscope, increasing the cases of damaged particles [40,41]. To prevent these issues, the main parameters to consider are the blotting conditions, which affect the ice thickness: blotting time, blotting force, chamber temperature, and humidity. These parameters can be controlled using commercially available plungers and are generally optimized through a trial-and-error procedure. Moreover, the type of sample support, the batch of grids, and the hydrophilicity of the support can affect ice thickness.

The most commonly used grids are the holey copper carbon, although recently, alternative grid designs have also been explored, such as coating carbon film with graphene [42,43], and the possibility of replacing the grid support and\or carbon film with gold [44].

3. Data collection

The frozen EM-grids are loaded into a cryo-electron microscope, a transmission electron microscope (TEM) designed to operate and keep the samples at liquid nitrogen temperature to collect cryo-EM datasets. Like any other TEM and optical microscope, a cryo-electron microscope's essential components are the beam source, a series of lenses, and an image acquisition system. The electrons are accelerated across the microscope column, and, unlike photons, they are massive and negatively charged, with a short wavelength proportionally inverse of the acceleration voltage (2.5 pm at 200 kV and 1.97 pm at 300 kV). However, the imperfection of the electromagnetic lenses pushes the resolution achievable far above the theoretical Bragg limits [45], but still higher than the one achievable in an optic microscope.

3.1. Electron microscope structure

Within the electron microscope, the available electron sources are represented by (i) a heated filament, (ii) a LaB6 crystal, and (iii) a field emission gun (FEG). Up to now, FEG is the widely used electron source because it emits coherent, near-monochromatic, and high-current density electrons [46]. The electron microscope lens system comprises condenser, objective, intermediate, and projector lenses (Figure 1A). The condenser lens or system is positioned just below the electron source and regulates the electron beam's size and focus on the sample. The condenser is associated with a condenser aperture that blocks the electrons with a large angular spread, improving the beam coherence. The objective lens, placed below the sample holder, forms the initial image and defines its quality. Variations in its electric field tune the focus of the image on the viewing screen or the detector. As previously described for the condenser lens, the objective lens is coupled with an objective lens aperture positioned between the sample holder and the objective lens. This aperture stops electrons from being widely scattered, increasing the contrast of the image. Notably, a system of lenses composed of the intermediate and projector lenses increases the image magnification before the electrons have reached the detector [47].
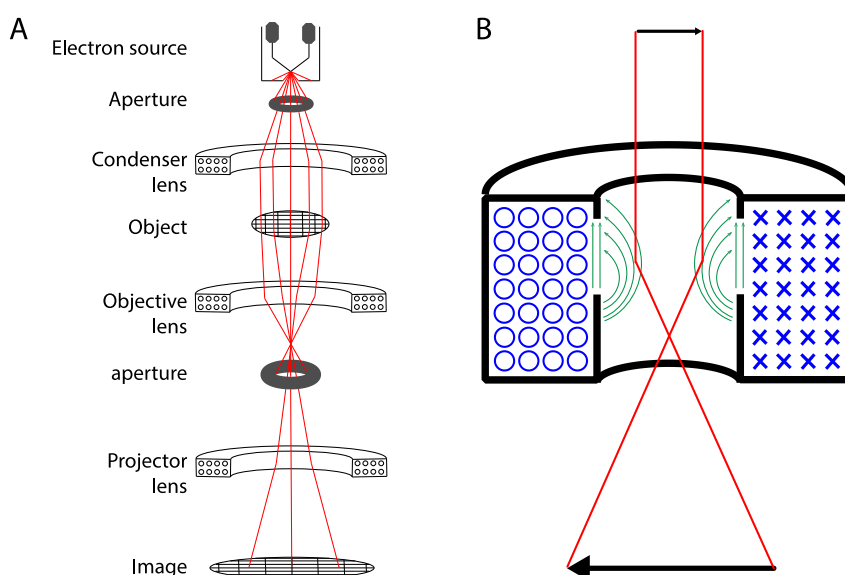

Figure 1. schematic representation of an electron microscope (A) and of an electromagnetic lens (B). The copper wires are in blue and the magnetic field is symbolized by green lines.

3.2. Defect of electromagnetic lens

Unlike optics lenses, electromagnetic lenses are composed of a coil of copper wires inside the iron pole pieces that generate a magnetic field that interacts with the electron beam, as described by the Lorentz force (Figure 1B). The manufacturing of these lenses is more complex and expensive than optical lenses, and it is processed defect prone. In particular, the defects that can substantially limit the performance of an electron microscope are the spherical and chromatic aberration of electromagnetic lenses and axial astigmatism.

The spherical aberration reflects the inability of the lens to focus all the incident rays from a point source to another point. This defect is caused by the magnetic fields of the lenses that unevenly act on the rays off-axis. In paraxial conditions, the rays are close to the lens axis and form only small angles; then, the more an electron is far from the lens axis, the smaller its focal distance. Therefore, a point-like object forms a discoidal image in the Gaussian image plane (Figure 2A). The radius (R_s) of this disc, called aberration disc, depends on the angular opening β, according to the expression $R_s = C_s\beta^3$, where C_s is the spherical aberration coefficient that, for typical TEM, is between 1 and 3 mm [48]. For an electromagnetic lens placed behind the objective lens, the aperture of the incident beam is smaller than the opening of the beam incident on the objective lens by a factor given by the magnification of this lens. This aberration could be partially counteracted by operating the lens under-focus mode [49].
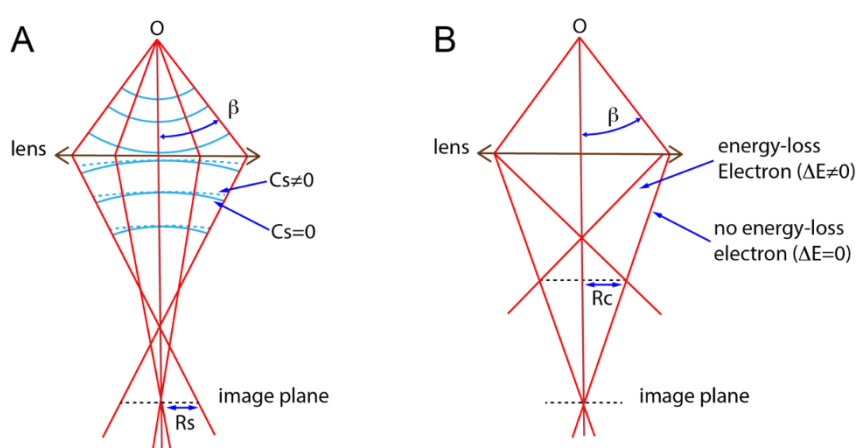

Figure 2. Representation of the effect of spherical aberration (A) and chromatic aberration (B).

The relevance of chromatic aberration arises when electrons vary in energy. Indeed, lenses strongly retain electrons with low energy, obtaining a disk in the plane of the Gaussian image starting from a point in the plane of the object. The R_c of this disc radius is given by the expression $R_c = C_c \Delta E \beta$, where C_c is the chromatic aberration coefficient, ΔE is the variation of the electron energy from its mean value E, and β is the opening angle of the lens (Figure 2A). The C_c of a magnetic lens usually has a slightly lower numerical value than the focal length [48]. This aberration degrades the image when the electrons in the beam stop being monoenergetic, and this can occur when (i) electrons are generated from the electron gun with a spread of energies, (ii) the acceleration voltages or currents in the coils fluctuate over time, or (iii) the electron beam loses energy through collisions, passing through a sample. In modern microscopes, the stability of the accelerating voltage and the current in the lens are well controlled, so they do not influence any more chromatic aberrations [48].

Axial astigmatism occurs when electrons go through a non-uniform magnetic field. This defect depends on the impossibility of making the iron of the lens that surrounds the coil (Figure 1B) perfectly cylindrical. The iron may also have microstructural defects that cause local variations in the magnetic field strength. Moreover, even if these difficulties are overcome, apertures introduced before the lens could disturb the field if they are not precisely centered around the axis of the lens. These contributions to astigmatism globally distort the image, and this distortion (R_a) can be described as $R_a = \beta\Delta f$, where Δf is the maximum difference in focus induced by astigmatism. However, axial astigmatism can be stabilized using appropriate corrector elements below the objective lens [48].

3.3. Image formation

The formation of the image into an electron microscope derives from the interaction of the electrons with the object. Electrons can either cross the sample as a transparent medium, be scattered without any energy loss (elastic scattering), or transfer part of their energy to the sample (inelastic scattering). Only the electrons that undergo inelastic scattering possess the appropriate phase shift necessary to form the image. In a biological context, the light atoms that mainly compose biological samples (mostly H, O, N and C) weakly interact with the incoming electrons, then a biological sample can be considered weak phase objects. Therefore, the contrast of an image derived from a biological sample is proportional to the projected object potential [50]. Taking into account the lens imperfection, the relationship between the image contrast $i(\vec{x})$ and the object projection $o(\vec{x})$ can be written as the convolution:

$$i(\vec{x}) = o(\vec{x}) \otimes P(\vec{x})$$

where $P(\vec{x})$ is the point spread function (PSF), which represent the microscope aberrations. Therefore, the Fourier transform of the image contrast $I(\vec{k}) = \mathcal{F}[I(\vec{x})]$ can be written as:

$$I(k) = O(k)C(k)E(k)$$

where $O(k)$ is the Fourier transform of the object projection, the function $C(k)$—also known as contrast transfer function (CTF)—mathematically describes how aberrations influence the image formation [51], and $E(k)$ is the envelope function, which takes into account the decay of the signal, due to spatial and temporal effects introduced by the microscope aberrations [47].
$C(k)$ can be written as:

$$C(k) = sin\left[\frac{2\pi}{\lambda}\left(\frac{Cs\lambda^4 k^4}{4} - \frac{\Delta z\lambda^2 k^2}{2}\right)\right]$$

where Δz is the defocus value, λ is the electron wavelength, Cs is the spherical aberration, and k indicate the spatial frequency. It is worth to be notice the role of the defocus value Δz to the image formation: a higher defocus increases the image contrast but, at the same time, reduces the achievable resolution. Indeed, collect data within a defocus range of -0.5 to -3 μm could be a good compromise.
$E(k)$ can be simplified by approximating it as a one parameter Gaussian function:

$$E(k) = e^{-Bk^2}$$

where B is the experimental B-factor [52]. It is important to note that, although B has the same form as the temperature factor used in X-ray crystallography, it does not have the same physical significance. Indeed, the experimental B-factor depends on the experimental conditions and microscope optics, while the X-ray crystallography temperature factor describes the vibration of the atoms within the crystals.

3.4. Image recording and acquisition

Along with technical improvements, detectors played a key role in the "resolution revolution".

The two most important parameters used to describe the performance of a detector are the Detective Quantum Efficiency (DQE) and the Modulation Transfer Function (MTF). DQE is defined as the ratio between the Signal to Noise Ratio (SNR) of the output image over the SNR of the input signal, showing how much the original signal can be degraded by the physics or the noise of the acquisition system [24]. In the case of a pixelated detector, the pixel spacing fixes the maximum spatial frequency in an image, which the detector can record since the shortest wavelength will be sampled at least twice. This discretization of the detector sets the so-called Nyquist cut-off frequency as 1/(2*pixel spacing) [46]. The MTF has been defined as the function-dependent ratio between the image contrast over the object contrast, describing how strongly the various spatial frequencies outside the Nyquist frequency are recorded. MTF depends on the detector pixel size and other detector design factors, such as the spreading of the electrons in the active layer of the detector. The first electron microscopes were equipped with photographic films [3], while later, films were replaced by digital detectors, avoiding the long delay between the exposure and the observation of the image. These digital detectors can be clustered into two-family: charged-coupled devices (CCD) and direct detector devices (DDD).

3.4.1. Charged-coupled devices (CCD)

The Charged-coupled devices (CCD) consist of an integrated circuit formed by a line or a grid of semiconductor elements that accumulate an electric charge proportional to the intensity of the incoming electromagnetic radiation. These elements are coupled, leading to the transfer of the charges between the neighboring pixels and the readout register, and then to their amplification and conversion into a digital signal [53]. In TEM, CCD are combined with a scintillator. Therefore, the incoming signal undergoes a two-step conversion, from electron to photon and photon to electron, reducing the spatial resolution, consequent to the multiple scattering of the light inside the scintillator. However, when cooled, a CCD has a good DQE (> 0.5) [46], and, compared to photographic films, the CCD camera has the advantage of a rapid readout real-time response and an extended dynamic range.

3.4.2. Direct detector devices (DDD)

Direct detector devices (DDD) were developed to avoid the intermediate light conversion step in the CCD. DDD is composed of an active pixel sensor based on complementary metal-oxide-semiconductor (CMOS), which can be directly exposed to the high-energy electron beam and detect the incoming electrons. An incident beam passes through a thin CMOS layer (150 μm [54]), leaving an ionization trail. The electron (or hole) generated in the semiconductor is accelerated to an adjacent contact, creating a signal. This phenomenon dramatically increases the SNR of the incoming signal and, therefore, the DQE, compared to CCD and photographic films [24,25].

Furthermore, the small thickness of the CMOS layer minimizes the ion trail and the lateral charge spread, resulting in higher spatial resolution than the CCD camera. A direct electron detector also has a high frame rate, with no dead time between frames. This high frame rate delivers intrinsic dose fractionation during image acquisition, which can be exploited for beam-induced motion correction [55,56], damage compensation, and other image processing techniques [22,57].

The analysis of a single particle cryo-EM dataset consists of reconstructing the 3D density map of the studied molecule, starting from a set of images representing the different 2D projections of the molecules deposited on a cryo-EM grid at various orientations [58]. The critical steps of this analysis

include the micrographs preprocessing, particle picking, the 2D classification, and the 3D reconstruction of the final density map (Figure 3).

4. Single particles 3D reconstruction

The analysis of a single particle cryo-EM dataset consists of reconstructing the 3D density map of the studied molecule, starting from a set of images representing the different 2D projections of the molecules deposited on a cryo-EM grid at various orientations [58]. The critical steps of this analysis include the micrographs preprocessing, particle picking, the 2D classification, and the 3D reconstruction of the final density map (Figure 3).
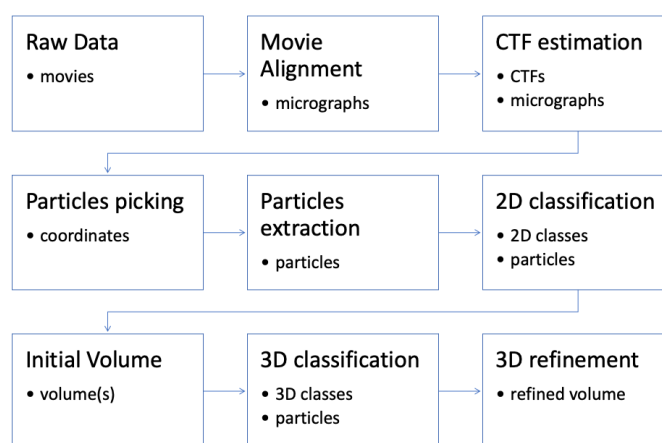
Figure 3. Simplified single particle cryo-EM data analysis workflow. Each step in the workflow indicates the corresponding output.

4.1. Micrographs preprocessing

4.1.1. Movie alignment

Using DDD cameras with a high image acquisition rate enabled the collection of multiple frame images of the exact exposition. However, DDD movies are typically acquired with a low exposure per frame (0.8 to 3 e$^-$/Å^2/frame), resulting in a low SNR in individual frames. These movies revealed that the electron beam could induce a sample motion that blurs the images [59,60]. Moreover, the beam-induced motion can not be described entirely as a rigid body translation [60] because the beam induces independent movements of ice-embedded proteins in each frame. Therefore, an optimal extraction of high-resolution density requires an accurate alignment of every frame to increase the SNR and trace these relative movements.

4.1.2. CTF estimation and correction

As shown previously (section 3.3), the CTF describes the effect of the microscope aberration on the image formation. Thus, accurate estimation and correction of the CTF are fundamental to obtain high-resolution cryo-EM structures.

Therefore, the parameters needed for the CTF determination, such as acceleration voltage, spherical aberration constant, acquisition defocus, axial astigmatism, magnification, and percentage of the amplitude contrast, are the primary descriptor of the microscope set up. The accelerating voltage and the spherical aberration are instrumental parameters, while the amplitude contrast is determined empirically, typically 10% for the modern cryo-EM microscope [47]. The defocus value is set to a nominal value during the images acquisition and determined subsequently with more precision during the CTF evaluation, together with the spherical aberration by minimizing the discrepancy between the calculated and the observed CTF. There are several software available to estimate CTF; the most used are EMAN [12], CTFFIND3 [61], CTFFIND4 [62], and GCTF [63]. Compare the results of more than one of these software to select only the micrographs with a correctly evaluated CTF (i.e., micrographs that do not present strong aberration or limitations to the resolution of the final reconstruction) could be a good strategy.

4.2. Two-dimensional classification

Two-dimensional classification is performed to obtain three significant results: (i) discard invalid particles selected during the particles picking; (ii) give a fast and semi-quantitative screen of the data quality, such as angular distribution of the particles view or particles homogeneity; and finally, (iii) provide high SNR particle averages, which can be used for automatic particles picking. During the 2D classification, the dataset is divided iteratively into a selected number of classes (K). Each iteration is composed of two steps. The first step computes the correlation between the template and each class image, assigning the images to the class with the most similar template to find the best match with the template. The second step calculates a new average from the K classes as a template for the next iteration (Figure 4). The main drawback of this classification approach is that the convergence can lead to a local minimum, not guaranteeing the global optimum classification achievement. This issue can be reduced with the maximum likelihood methodology [64,65], in which each particle can be assigned to more than one class with a weighting factor.
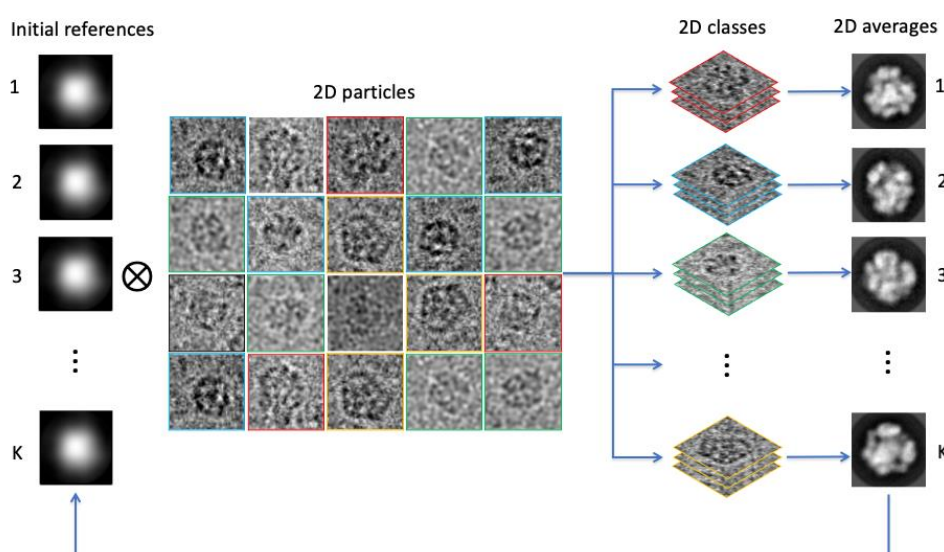

Figure 4. Schematic representation of a 2D classification iteration. Data are extracted from [66].

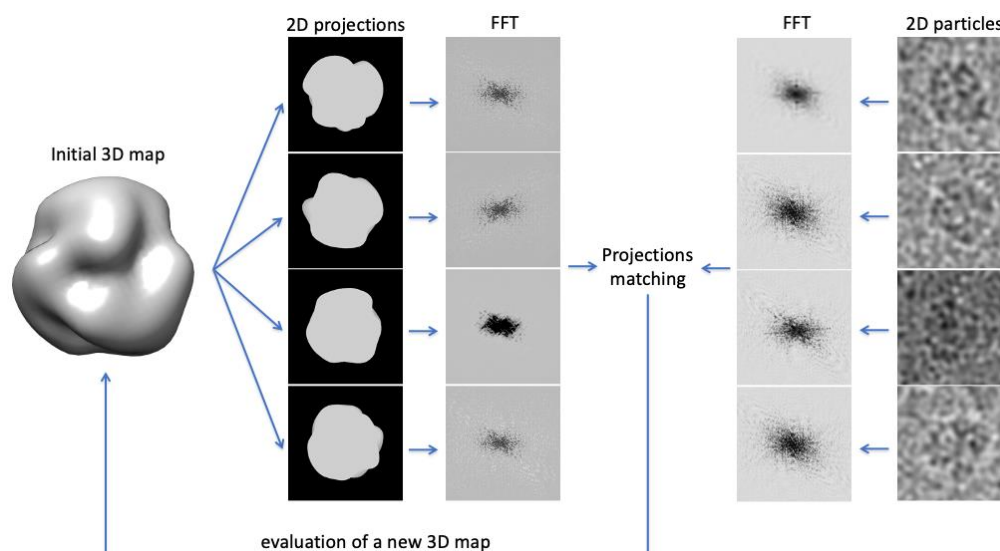## 4.3. Three-dimensional classification

Figure 5. Schematic representation of a 3D reconstruction iteration.

The reconstruction of a 3D object from its 2D projections is performed in the Fourier space, taking advantage of the projection theorem, which postulates that each 2D projection of a 3D object is the central section of the object 3D Fourier transform. Consequently, a 3D reconstruction can be obtained from a 3D inverse Fourier transformation of the 3D Fourier domain, composed of the 2D Fourier sections [47,67]. The 3D reconstruction is based, once again, on the iteration of two steps: in the first one, the particles are compared with the re-projection of the calculated 3D reconstruction, and the orientation with the best cross-correlation value indicates the favorite projection direction (Figure 5). In the second, a new 3D map is computed using the updated angular projection parameters provided by the first step. The most significant advantage of cryo-EM is its ability to distinguish the studied molecules' differential structural states. Then, trace these different conformational states using a maximum-likelihood approach, similar to the one used for the 2D classification. Whereas the conventional alignment approach aims to find the unique optimal parameters (in-plane rotations and translations) for each image, the maximum-likelihood approach integrates over the probability distributions of all possible values. Thus, it assigns several in-plane orientation values to each image with proper weights [65]. A variant of this statistical method is an empirical Bayesian approach [17,68]. The difference between these two methods lies in a regularization parameter that weights the prior knowledge about the 3D reconstruction:

$$P(\Theta|X,Y) \propto P(X|\Theta,Y)P(\Theta|Y),$$

where $P(X|\Theta,Y)$ is the likelihood that describes the probability of observing the data, given the model with parameter set Θ. $P(\Theta|Y)$ expresses how likely that parameter set Θ is, given the prior 3D information. The method of optimizing the posterior distribution $P(\Theta|X,Y)$ is called maximum a posteriori estimation (MAP), whereas optimizing the likelihood $P(X|\Theta,Y)$ is the maximum likelihood estimation. In the 3D classification context, X represents the particles set $X = \{X_1, X_2, \ldots X_N\}$, where N is the total number of particles, and $\Theta = \{V_1, V_2, \ldots, V_K\}$ is the set of different

volumes, where K is the given number of classes in which the dataset is divided.

4.4. Structure refinement and resolution assessment

The maps resulting from the 3D classification initial needs to be refined to obtain a final map with better details. The refinement procedure is based on the same algorithm of the 3D classification, putting K = 1. During the refinement, the dataset is divided into two independent halves that were reconstructed separately. At the end of each reconstruction iteration, the cross-correlation over spatial frequency shells is calculated, with an increasing radius between the Fourier transforms of the two-independent reconstructions (Figure 6). This process is known as Fourier shell correlation (FSC) [47,69]. At the end of the refinement, the quality of the 3D map is possible to numerically describe by the resolution, i.e., the resolvability of object details in the density map. The resolution is obtained by comparing the measured FSC and a threshold value [70,71]. The FSC = 0.143 threshold, proposed by Rosenthal and Henderson [71], was chosen by comparing the cryo-EM results with the resolution of the same structures determined by X-ray crystallography [72]. This method is the most commonly used, represents an overall resolution, and gives only a general idea of the quality of the map since different regions can have substantially different values of local resolution. Therefore, a good practice is to use structural features, which confirm the resolution given by FSC. For example, in a low-resolution protein map (> 10 Å), it is possible to distinguish only the overall profile of the structure, while a mid-resolution map (4–10 Å) reveals the secondary structure and the relative arrangements of the domains. Then, a near-atomic resolution map (< 4 Å) clearly shows the polypeptide backbone trace and most amino acid side chains. However, the numerical meaning of the resolution is still under debate in the cryo-EM field, and different approaches to its evaluation can be used.
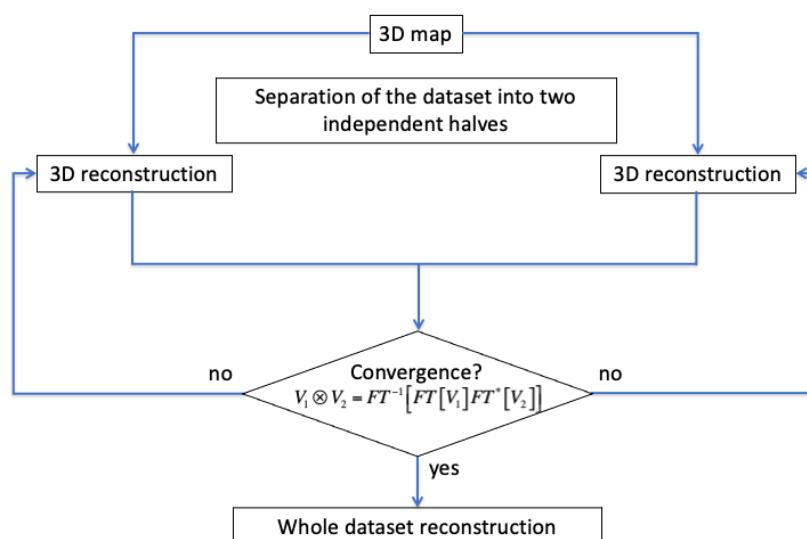

Figure 6. Schematic representation of the 3D refinement procedure.

5.   Conclusions

The use of cryo-EM to determinate biological structures has undergone impressive growth in the

latest decade and today represents a valid candidate both to solve macromolecular complexes by fitting already known structures into low-resolution maps and obtaining de-novo high-resolution reconstructions.

Compared to the classical techniques employed for structural biology, such as crystallography and NMR, cryo-EM can be easily adapted to different samples because it does not usually require previous sample manipulation, such as crystallization. The first significant advantage of using cryo-EM for structure determination is that depside other structural techniques often provides some structural insight regardless of the achieved overall resolution. This is because, even at lower resolutions, cryo-EM maps can show higher local resolution regions with secondary structural features, such as α-helices and β-sheets or, in the worst case, a low-resolution molecular envelope of the sample. Thanks to all these things, cryo-EM is becoming an increasingly used technique and, although high resolution is still not achievable systematically, the deposited structures obtained with cryo-EM are growing exponentially. Despite its recent development, cryo-EM can already be a mature technology, but it still enjoys a vigorous innovative drive. The continuous optimization and automation of its necessary steps will lead to an ever-greater use of cryo-EM, and it could soon become the main technique in structural biology.

Acknowledgments

Conflict of interest

The authors declare no conflict of interest.

Author contributions:

AG concepted and designed the work, draft the article. VR edited and revised the manuscript.

References

1. Murata K, Wolf M (2018) Cryo-electron microscopy for structural analysis of dynamic biological macromolecules. *Biochim Biophys Acta-Gen Subj* 1862: 324–334. https://doi.org/10.1016/j.bbagen.2017.07.020
2. Zanotti G, Grinzato A (2021) Structure of filamentous viruses. *Curr Opin Virol* 51: 25–33. https://doi.org/10.1016/j.coviro.2021.09.006
3. Ruska E (1987) The development of the electron microscope and of electron microscopy. *Biosci Rep* 7: 607–629. https://doi.org/10.1007/BF01127674
4. Brenner S, Horne RW (1959) A negative staining method for high resolution electron microscopy of viruses. *Biochim Biophys Acta* 34: 103–110. https://doi.org/10.1016/0006-3002(59)90237-9
5. Von Borries B, Ruska E, Ruska H (1938) Bakterien und virus in übermikroskopischer aufnahme. *Klin Wochenschr* 17: 921–925. https://doi.org/10.1007/BF01775798
6. Kausche GA, Pfankuch E, Ruska H (1939) Die sichtbarmachung von pflanzlichem virus im Übermikroskop. *Naturwissenschaften* 27: 292–299. https://doi.org/10.1007/BF01493353

7. Dubochet J, McDowall AW (1981) Vitrification of pure water for electron microscopy. *J Microsc* 124: 3–4.

8. Dubochet J, Lepault J, Freeman R, et al. (1982) Electron microscopy of frozen water and aqueous solutions. *J Microsc* 128: 219–237. https://doi.org/10.1111/j.1365-2818.1982.tb04625.x

9. Dubochet J, Adrian M, Chang JJ, et al. (1988) Cryoelectron microscopy of vitrified specimens. *Q Rev Biophys* 21: 129–228.

10. Frank J, Shimkin B, Dowse H (1981) SPIDER—a modular software system for electron image processing. *Ultramicroscopy* 6: 343–357. https://doi.org/10.1142/9789813234864_0008

11. Van Heel M, Frank J (1981) Use of multivariates statistics in analysing the images of biological macromolecules. *Ultramicroscopy* 6: 187–194. https://doi.org/10.1016/S0304-3991(81)80197-0

12. Ludtke SJ, Baldwin PR, Chiu W (1999) EMAN: semiautomated software for high-resolution single-particle reconstructions. *J Struct Biol* 128: 82–97. https://doi.org/10.1006/jsbi.1999.4174

13. Sorzano COS, Marabini R, Velázquez-Muriel J, et al. (2004) XMIPP: a new generation of an open-source image processing package for electron microscopy. *J Struct Biol* 148: 194–204. https://doi.org/10.1016/j.jsb.2004.06.006

14. Suloway C, Pulokas J, Fellmann D, et al. (2005) Automated molecular microscopy: the new Leginon system. *J Struct Biol* 151: 41–60. https://doi.org/10.1016/j.jsb.2005.03.010

15. Tang G, Peng L, Baldwin PR, et al. (2007) EMAN2: an extensible image processing suite for electron microscopy. *J Struct Biol* 157: 38–46. https://doi.org/10.1016/j.jsb.2006.05.009

16. Lander GC, Stagg SM, Voss NR, et al. (2009) Appion: an integrated, database-driven pipeline to facilitate EM image processing. *J Struct Biol* 166: 95–102. https://doi.org/10.1016/j.jsb.2009.01.002

17. Scheres SHW (2012) RELION: implementation of a Bayesian approach to cryo-EM structure determination. *J Struct Biol* 180: 519–530. https://doi.org/10.1016/j.jsb.2012.09.006

18. Grigorieff N, Grant T, Rohou A (2017) cisTEM: user-friendly software for single-particle image processing. *Acta Crystallogr Sect A* 73: C1368–C1368.

19. Punjani A, Rubinstein JL, Fleet DJ, et al. (2017) CryoSPARC: Algorithms for rapid unsupervised cryo-EM structure determination. *Nat Methods* 14: 290–296. https://doi.org/10.1038/nmeth.4169

20. Conesa Mingo P, Gutierrez J, Quintana A, et al. (2018) Scipion web tools: Easy to use cryo-EM image processing over the web. *Protein Sci* 27: 269–275. https://doi.org/10.1002/pro.3315

21. Kimanius D, Forsberg BO, Scheres SHW, et al. (2016) Accelerated cryo-EM structure determination with parallelisation using GPUs in RELION-2. *Elife* 5: 1–21. https://doi.org/10.7554/eLife.18722.001

22. Luecken U, Van HG, Schuurmans F, et al. (2011) Method of using a direct electron detector for a TEM.

23. Milazzo AC, Cheng A, Moeller A, et al. (2011) Initial evaluation of a direct detection device detector for single particle cryo-electron microscopy. *J Struct Biol* 176: 404–408. https://doi.org/10.1016/j.jsb.2011.09.002

24. Ruskin RS, Yu Z, Grigorieff N (2013) Quantitative characterization of electron detectors for transmission electron microscopy. *J Struct Biol* 184: 385–393. https://doi.org/10.1016/j.jsb.2013.10.016

25. Kuijper M, van Hoften G, Janssen B, et al. (2015) FEI's direct electron detector developments: Embarking on a revolution in cryo-TEM. *J Struct Biol* 192: 179–187. https://doi.org/10.1016/j.jsb.2015.09.014

26. Ripstein ZA, Rubinstein JL (2016) Processing of Cryo-EM movie data, *Methods in Enzymology*, Elsevier Inc., 103–124. https://doi.org/10.1016/bs.mie.2016.04.009

27. Li X, Mooney P, Zheng S, et al. (2013) Electron counting and beam-induced motion correction enable near-atomic-resolution single-particle cryo-EM. *Nat Methods* 10: 584–590. https://doi.org/10.1038/nmeth.2472

28. Kühlbrandt W (2014) The resolution revolution. *Science* 343: 1443–1444. https://doi.org/10.1126/science.1251652

29. Bai XC, McMullan G, Scheres SHW (2015) How cryo-EM is revolutionizing structural biology. *Trends Biochem Sci* 40: 49–57. https://doi.org/10.1016/j.tibs.2014.10.005

30. Lawson CL, Patwardhan A, Baker ML, et al. (2016) EMDataBank unified data resource for 3DEM. *Nucleic Acids Res* 44: D396-403. https://doi.org/10.1093/nar/gkv1126

31. Nakane T, Kotecha A, Sente A, et al. (2020) Single-particle cryo-EM at atomic resolution. *Nature* 587: 152–156. https://doi.org/10.1038/s41586-020-2829-0

32. Weis F, Beckers M, von der Hocht I, et al. (2019) Elucidation of the viral disassembly switch of tobacco mosaic virus. *EMBO Rep* 20: e48451. https://doi.org/10.15252/embr.201948451

33. Grinzato A, Kandiah E, Lico C, et al. (2020) Atomic structure of potato virus X, the prototype of the Alphaflexiviridae family. *Nat Chem Biol* 16: 564–569. https://doi.org/10.1038/s41589-020-0502-4

34. Masuyer G, Conrad J, Stenmark P (2017) The structure of the tetanus toxin reveals pH-mediated domain dynamics. *EMBO Rep* 18: 1306–1317. https://doi.org/10.15252/embr.201744198

35. Pirazzini M, Grinzato A, Corti D, et al. (2021) Exceptionally potent human monoclonal antibodies are effective for prophylaxis and therapy of tetanus in mice. *J Clin Invest* 131: e151676. https://doi.org/10.1172/JCI151676.

36. Sobti M, Smits C, Wong ASW, et al. (2016) Cryo-EM structures of the autoinhibited E. coli ATP synthase in three rotational states. *Elife* 5: e21598. https://doi.org/10.7554/eLife.21598.001

37. Skiniotis G, Southworth DR (2016) Single-particle cryo-electron microscopy of macromolecular complexes. *Microscopy* 65: 9–22. https://doi.org/10.1093/jmicro/dfv366

38. Chen JZ, Sachse C, Xu C, et al. (2008) A dose-rate effect in single-particle electron microscopy. *J Struct Biol* 161: 92–100. https://doi.org/10.1016/j.jsb.2007.09.017

39. Cho H, Hyun J, Kim J, et al. (2013) Measurement of ice thickness on vitreous ice embedded cryo-EM grids: investigation of optimizing condition for visualizing macromolecules. *J Anal Sci Technol* 4: 7. https://doi.org/10.1186/2093-3371-4-7

40. Glaeser RM (2018) Proteins, interfaces, and cryo-EM grids. *Curr Opin Colloid Interface Sci* 34: 1–8. https://doi.org/10.1016/j.cocis.2017.12.009

41. D'Imprima E, Floris D, Joppe M, et al. (2019) Protein denaturation at the air-water interface and how to prevent it. *Elife* 8: e42747. https://doi.org/10.7554/eLife.42747.001

42. Pantelic RS, Suk JW, Magnuson CW, et al. (2011) Graphene: substrate preparation and introduction. *J Struct Biol* 174: 234–238. https://doi.org/10.1016/j.jsb.2010.10.002

43. Russo CJ, Passmore LA (2014) Controlling protein adsorption on graphene for cryo-EM using low-energy hydrogen plasmas. *Nat Methods* 11: 649–652. https://doi.org/10.1038/nmeth.2931

44. Russo CJ, Passmore LA (2014) Ultrastable gold substrates for electron cryomicroscopy. *Science* 346: 1377–1380. https://doi.org/10.1126/science.1259530

45. Glaeser RM (1979) Prospects for extending the resolution limit of the electron microscope. *J Microsc* 117: 77–91. https://doi.org/10.1111/j.1365-2818.1979.tb00232.x

46. Williams DB, Carter CB (2009) *Transmission Electron Microscopy: A Textbook for Materials Science*.

47. Frank J (2006) Three-dimensional electron microscopy of macromolecular assemblies: visualization of biological molecules in their native state, Oxford University Press.

48. Williams DB, Carter CB (2009) Planar defects, *Transmission Electron Microscopy*, Boston: Springer, 419–439. https://doi.org/10.1007/978-0-387-76501-3_25

49. Williams DB, Carter CB (2009) Phase-contrast images, *Transmission Electron Microscopy*, 389–405. https://doi.org/10.1007/978-0-387-76501-3_23

50. Wade RH (1992) A brief look at imaging and contrast transfer. *Ultramicroscopy* 46: 145–156. https://doi.org/10.1016/0304-3991(92)90011-8

51. Kohl H, Reimer L (2008) *Transmission Electron Microscopy: Physics of Image Formation*, Springer-Verlag New York. https://doi.org/10.1007/978-0-387-40093-8

52. Saad A, Ludtke SJ, Jakana J, et al. (2001) Fourier amplitude decay of electron cryomicroscopic images of single particles and effects on structure determination. *J Struct Biol* 133: 32–42. https://doi.org/10.1006/jsbi.2001.4330

53. Faruqi AR, Subramaniam S (2000) CCD detectors in high-resolution biological electron microscopy. *Q Rev Biophys* 33: 1–27. https://doi.org/10.1017/S0033583500003577

54. Meyer R, Kirkland A (2007) Direct electron detector.

55. Li X, Mooney P, Zheng S, et al. (2013) Electron counting and beam-induced motion correction enable near-atomic-resolution single-particle cryo-EM. *Nat Methods* 10: 584–590. https://doi.org/10.1038/nmeth.2472

56. Scheres SHW (2014) Beam-induced motion correction for sub-megadalton cryo-EM particles. *Elife* 3: e03665. https://doi.org/10.7554/eLife.03665.001

57. Shigematsu H, Sigworth FJ (2013) Noise models and cryo-EM drift correction with a direct-electron camera. *Ultramicroscopy* 131: 61–69. https://doi.org/10.1016/j.ultramic.2013.04.001

58. Nogales E (2016) The development of cryo-EM into a mainstream structural biology technique. *Nat Methods* 13: 24–27. https://doi.org/10.1038/nmeth.3694

59. McMullan G, Faruqi AR (2008) Electron microscope imaging of single particles using the Medipix2 detector. *Nucl Instruments Methods Phys Res Sect A Accel Spectrometers, Detect Assoc Equip* 591: 129–133. https://doi.org/10.1016/j.nima.2008.03.041

60. Brilot AF, Chen JZ, Cheng A, et al. (2012) Beam-induced motion of vitrified specimen on holey carbon film. *J Struct Biol* 177: 630–637. https://doi.org/10.1016/j.jsb.2012.02.003

61. Mindell JA, Grigorieff N (2003) Accurate determination of local defocus and specimen tilt in electron microscopy. *J Struct Biol* 142: 334–347. https://doi.org/10.1016/S1047-8477(03)00069-8

62. Rohou A, Grigorieff N (2015) CTFFIND4: Fast and accurate defocus estimation from electron micrographs. *J Struct Biol* 192: 216–221. https://doi.org/10.1016/j.jsb.2015.08.008

63. Zhang K (2016) Gctf: Real-time CTF determination and correction. *J Struct Biol* 193: 1–12. https://doi.org/10.1016/j.jsb.2015.11.003

64. MacKay DJC (2003) *Information Theory, Inference and Learning Algorithms*, Cambridge university press.

65. Sigworth FJ, Doerschuk PC, Carazo JM, et al. (2010) An introduction to maximum-likelihood methods in cryo-EM. *Methods Enzym* 482: 263–294. https://doi.org/10.1016/S0076-6879(10)82011-7

66. Zarzecka U, Grinzato A, Kandiah E, et al. (2020) Functional analysis and cryo-electron microscopy of Campylobacter jejuni serine protease HtrA. https://doi.org/10.1080/19490976.2020.1810532

67. Orlova EV, Saibil HR (2011) Structural analysis of macromolecular assemblies by electron microscopy. *Chem Rev* 111: 7710–7748. https://doi.org/10.1021/cr100353t

68. Scheres SHW (2012) A Bayesian view on cryo-EM structure determination. *J Mol Biol* 415: 406–418. https://doi.org/10.1016/j.jmb.2011.11.010

69. Liao HY, Frank J (2010) Definition and estimation of resolution in single-particle reconstructions. *Structure* 18: 768–775. https://doi.org/10.1016/j.str.2010.05.008

70. Böttcher B, Wynne SA, Crowther RA (1997) Determination of the fold of the core protein of hepatitis B virus by electron cryomicroscopy. *Nature* 386: 88–91. https://doi.org/10.1038/386088a0

71. Rosenthal PB, Henderson R (2003) Optimal determination of particle orientation, absolute hand, and contrast loss in single-particle electron cryomicroscopy. *J Mol Biol* 333: 721–745. https://doi.org/10.1016/j.jmb.2003.07.013

72. Henderson R, Sali A, Baker ML, et al. (2012) Outcome of the first electron microscopy validation task force meeting. *Structure* 20: 205–214.